

Modeling of dielectric barrier discharge plasma actuator

Cite as: J. Appl. Phys. **103**, 053304 (2008); <https://doi.org/10.1063/1.2841450>

Submitted: 28 September 2007 . Accepted: 04 December 2007 . Published Online: 11 March 2008

Balaji Jayaraman, Young-Chang Cho, and Wei Shyy



View Online



Export Citation

ARTICLES YOU MAY BE INTERESTED IN

[Modeling of dielectric barrier discharge plasma actuator in air](#)

Journal of Applied Physics **103**, 053305 (2008); <https://doi.org/10.1063/1.2837890>

[Electrohydrodynamic force and aerodynamic flow acceleration in surface dielectric barrier discharge](#)

Journal of Applied Physics **97**, 103307 (2005); <https://doi.org/10.1063/1.1901841>

[Modeling of dielectric barrier discharge plasma actuators driven by repetitive nanosecond pulses](#)

Physics of Plasmas **14**, 073501 (2007); <https://doi.org/10.1063/1.2744227>

Ultra High Performance SDD Detectors



See all our XRF Solutions

Modeling of dielectric barrier discharge plasma actuator

Balaji Jayaraman,^{a)} Young-Chang Cho, and Wei Shyy

Department of Aerospace Engineering, University of Michigan, Ann Arbor, Michigan 48109-2140, USA

(Received 28 September 2007; accepted 4 December 2007; published online 11 March 2008)

Glow discharge at atmospheric pressure using a dielectric barrier discharge can induce fluid flow and operate as an actuator for flow control. In this paper, we simulate the physics of a two-dimensional asymmetric actuator operating in helium gas using a high-fidelity first-principles-based numerical modeling approach to help improve our understanding of the physical mechanisms associated with such actuators. Fundamentally, there are two processes in the two half-cycles of the actuator operation, largely due to the difference in mobility between faster electrons and slower ions, and the geometric configurations of the actuator (insulator and electrodes). The first half-cycle is characterized by the deposition of the slower ion species on the insulator surface while the second half-cycle by the deposition of the electrons at a faster rate. A power-law dependence on the voltage for the resulting force is observed, which indicates that larger force can be generated by increasing the amplitude. Furthermore, one can enhance the effectiveness of the actuator by either increasing the peak value of the periodic force generation or by increasing the asymmetry between the voltage half-cycles or both. Overall, the increase in the lower electrode size, applied voltage, and dielectric constant tends to contribute to the first factor, and the decrease in frequency of applied voltage tends to contribute to the second factor. However, the complex interplay between the above factors determines the actuator performance. © 2008 American Institute of Physics. [DOI: 10.1063/1.2841450]

I. INTRODUCTION

Glow discharge at atmospheric pressure using a dielectric barrier discharge can induce fluid flow and operate as an actuator for flow control.^{1–6} The largely isothermal surface plasma generation realized above can modify the near-wall flow structure by means of Lorentzian collisions between the ionized fluid and the neutral fluid. Such an actuator has advantages of no moving parts, performance at atmospheric conditions, and devising complex control strategies through the applied voltage. However, the mechanism of the momentum coupling between the plasma and the fluid flow is not yet adequately understood which has fostered in recent times, a flurry of computational research activity toward deciphering the operating mechanisms and attempts to improve the present designs. Numerous applications including separation control at high angles of attack,¹ aerodynamic noise reduction⁷ and surface heat transfer enhancement⁸ have been adopted widely in the context of both low speed and high speed flow applications.^{9,10} A schematic illustration of an asymmetric actuator arrangement altering the near-wall flow is shown in Fig. 1.

Although these research studies indicate a wide range of application, the flow induced by the plasma actuator remains applicable predominantly in the low speed region. Even with various attempts with diverse geometries and applied voltages, the maximum flow velocity in the region of 5 m/s with 10 kV applied voltage for a single electrode pair although with peristaltic arrangements,¹¹ an array of single actuators, the induced flow achieves an order of magnitude increase. Improving the performance with minimal power is important

to broaden the application scope of the plasma actuator. These actuators typically operate on low power consumption (2–40 W/ft of wing span¹²) with the capability to be operated either in a continuous or pulsed fashion. It is reported¹² that the unsteady pulsed actuation of the discharge results in 90% less power consumption as compared to a steady actuation.

In the parametric investigations of a single actuator, Van Dyken *et al.*¹³ mentioned the waveform shape and dielectric thickness as the primary parameters affecting performance. Distinguishing the one atmosphere uniform glow discharge plasma and the dielectric barrier discharge (DBD), Roth *et al.*² state that the efficiency of producing plasma can be maximized at the Stoletow point (it is the point at which ionization happens with minimum energy requirement) in which a uniform, large volume plasma is realized.¹⁴ It has been documented¹² that the power approximately varies as the cube of applied voltage, but the induced flow saturates at

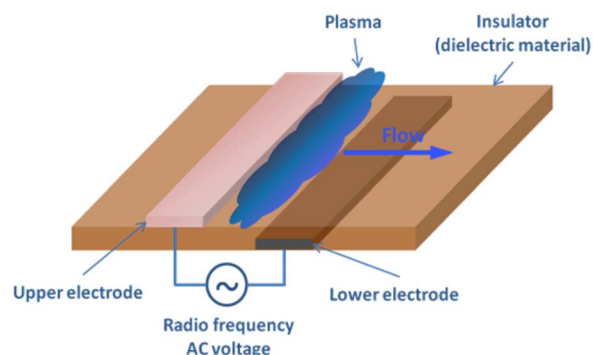


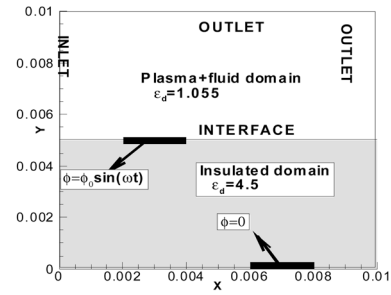
FIG. 1. (Color online) Illustration of glow discharge and induced flow.

^{a)}Electronic mail: jayaramanbalaji@gmail.com.

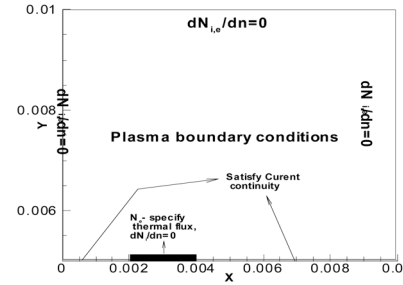
higher voltages when the discharge transitions from a weakly ionized to the corona/streamer mode. The performance of the actuator is also heavily dependent on the choice of dielectric material: quartz and Teflon® are known to produce the highest induced flow velocity with the least input power. Pons *et al.*¹⁵ in their experimental work analyzed the impact of the voltage frequency and magnitude along with the dielectric material thickness and conclude that a higher permittivity results in a higher velocity and larger power consumption.

In order to enhance the efficiency of the plasma actuator, it is important to investigate the DBD operating parameters by examining the dominant physical mechanisms. First-principles-based modeling of the detailed plasma dynamics in conjunction with the low-speed fluid dynamics has been developed by the present authors¹⁶ and in other parallel efforts.^{17–21} Computationally, the combined discharge physics and thermofluid transport modeling is a challenging problem due to the multiple nonlinear partial differential equations with strong source terms, and widely distributed length and time scales. The disparate length and time scales make the system computationally stiff, often requiring that numerical simulations be conducted with very small time-step sizes.¹⁶ Previously, a simpler model which is phenomenological in nature has been devised,¹⁸ where the approach is based on a linear field solution satisfying the governing equations with the model parameter being closed by observed experimental data. This model has been employed in many recent modeling studies.²² In order to offer a more comprehensive predictive capability, the present paper offers a refined treatment by accounting for the plasma physics based on the first-principles approach to establish correlations between the actuator performance and the design parameters. Similar efforts have also been undertaken,^{17,21,23} which complement our approach and employ a simplified chemistry for Helium gas. Over the last year, studies have been undertaken to assess the impact of the negative ions (Boeuf *et al.*²⁴) in the chemistry, especially when modeling air type mixtures. Singh and Roy²⁵ used an eight species chemistry for air modeling in his most recent article, while Likhanskii *et al.*^{26–28} employed a four-species chemistry while considering the major contributions. The latter focuses on the development of a more efficient nanosecond pulse driven DBD (Ref. 32) and the resultant unsteady flow field is compared with experiments.²⁸ Alternatively, Font *et al.*²⁹ used a hybrid particle-in-cell and Monte Carlo method to model the plasma and fluid flow.

However, the experimental evidence to validate the computational models is insufficient at this time and cross evaluations between the various studies are needed. The present approach, based on a different numerical framework, independently investigates the modeling parameters and transport property variations using the same model as that adopted from Roy and co-workers.^{17,21,23} In particular, we examine the interplay between the DBD operating parameters and the performance outcome. Specifically, we present the numerical results for the two-dimensional (2D) asymmetric actuator (Fig. 2), operating in helium gas, using the governing equations and the modeling approach summarized in the following sections. Following this, the characteristics of the actua-



(a) Complete domain with insulator indicating boundary conditions for fluid flow



(b) Top half of the domain indicating boundary conditions for plasma species and the region where the results are presented.

FIG. 2. (Color online) A representative 2D asymmetric discharge arrangements.

tor in terms of the net force generation, and associate plasma features are presented by varying the parameters such as applied voltage, frequency, actuator geometry, input voltage waveform, etc. The results reported in this study complement those referred to above, and offer added insight into the physical mechanisms and performance trends of the DBD actuator.

II. NUMERICAL MODEL

A. Plasma-fluid model

The fluid model for modeling the DBD consists of the first few moments of the Boltzmann equation for the various species with a near-Maxwellian distribution function. The plasma is considered as a multicomponent fluid comprised of two types of primary species, namely, ions and electrons (represented by subscripts *i* and *e*, respectively). Here, *n* and *v* represent the species number density and velocity, respectively.

Continuity equation.

Electrons:

$$\frac{\partial n_e}{\partial t} + \nabla \cdot (n_e v_e) = n_e S_{ie} - r n_i n_e. \quad (1)$$

Ions:

$$\frac{\partial n_i}{\partial t} + \nabla \cdot (n_i v_i) = n_e S_{ie} - r n_i n_e. \quad (1')$$

Here, the source terms on the right hand side represent the ionization/recombination processes which result in the creation (*S*) or destruction (*r*) of the species, as applicable.

TABLE I. Summary of property models employed for the He discharge simulation. Note that data are same as presented in Ref. 23.

Transport/reaction properties	Models/values employed
μ_i (ion mobility)	$= \frac{8 \times 10^3}{p \sqrt{E/p}} (1 - 8 \times 10^{-3} E/p) \text{ cm}^2 \text{ V}^{-1} \text{ s}^{-1} \text{ for } E/p \leq 25 \text{ V cm}^{-1} \text{ torr}^{-1}$ $= \frac{4.1 \times 10^4}{p \sqrt{E/p}} \left(1 - \frac{27.44}{(E/p)^{1.5}} \right) \text{ cm}^2 \text{ V}^{-1} \text{ s}^{-1} \text{ for } E/p > 25 \text{ V cm}^{-1} \text{ torr}^{-1}$
μ_e (electron mobility)	$= \frac{e}{m_e v_{en}} \text{ cm}^2 \text{ V}^{-1} \text{ s}^{-1}$, where $v_{en} = 10^{12} \text{ s}$
S_{ie} (species ionization model)	$= 4.4 \exp\left(\frac{-14}{(E/p)^{0.4}}\right) p \mu_e E \text{ s}^{-1}$
r (recombination coefficient)	$= 1.09 \times 10^{-20} T^{-9/2} n_e \text{ m}^3/\text{s}$
D_i (ion diffusivity)	$= 500 \text{ cm}^2/\text{s}$
D_e (electron diffusivity)	$= \frac{kT_e}{e} \mu_e \text{ cm}^2/\text{s}$
μ (viscosity of He gas)	$= 2.0 \times 10^{-5} \text{ N s/m}^2$

Momentum equation. The momentum equation for the species at high pressures (atmospheric conditions) can be reduced to the drift-diffusion form.³⁰ Here, μ and D represent the species mobility and diffusivity, respectively. The drift component of the momentum is the product of the mobility and the electric field E .

Electrons:

$$n_e \mu_e E - \nabla(n_e D_e) = n_e v_e. \quad (2)$$

Ions:

$$n_i \mu_i E - \nabla(n_i D_i) = n_i v_i. \quad (3)$$

As long as the thermal velocity is comparable to the drift velocity and we are in the continuum regime [Knudsen number (Kn) is low ($\lambda/L = \text{Kn} \ll 1$)], as the mean free path (λ) at atmospheric conditions is $O(10^{-7} \text{ m})$ and the actuator characteristic length (L) is $O(10^{-3} \text{ m})$, the inertial components in the momentum equation can be neglected. What is realized is a balance between the collision/ionization effects and the drift-diffusion components instead of the full momentum equation.³¹

The electric field equation. The electric field E is obtained using the solution of the Poisson equation, given by

$$\nabla \cdot (\epsilon_d E) = \frac{e(n_i - n_e)}{\epsilon_0}, \quad (4)$$

where ϵ_d and ϵ_0 are the dielectric constant and permittivity of free space.

B. Solution algorithm

The above set of equations is solved using a predictor-corrector-type approach for enhanced coupling between the dependent variables. The multiple scales arising from the ionized species chemistry are treated using a semi-implicit method for source terms. Specifically, an operator-split algorithm is embedded as a part of a projection method to enhance coupling between the various species equations being

solved. The detailed description of the solution approach is presented in our earlier work^{16,31,32} and hence we will only provide a broad overview of our approach. At the beginning of each time step, we solve for a predictor step to obtain an estimate for the species number densities using the lagged electric field values. The next step involves the solution of the Poisson equation using the predicted number densities to calculate the source terms. However, in our approach, we solve a semi-implicit version of the Poisson equation [Eq. (5)] to overcome the space charge stability constraint leading to the dielectric relaxation time-step constraint. This time step restriction is usually one of the most severe and is equivalent to the Courant type stability criterion for the current continuity equation. The origin of the restriction has been discussed in detail in our earlier work³¹ and is primarily caused by the nonimplicit treatment of the electric field in the species transport equations (predictor step). In order to overcome this, a linearized implicit treatment for the species number densities is used³¹ in the source term of the Poisson equation. By performing appropriate substitutions for the source term using the species transport equations, one will realize a right hand side that contains terms with the velocity and hence the electric field (through the drift-diffusion form of the momentum equation). By treating these terms implicitly, we can overcome the dielectric relaxation time step restriction. In the event, the full species momentum equations are solved instead of the drift-diffusion form; the predicted velocity thus obtained will be used in the Poisson equation. In that case, the nonlinearity will be difficult to overcome and will need a Newton–Raphson-type treatment. The modified Poisson equation leads to a symmetric system for the electric potential which needs to be inverted. This can be done using various linear system solution techniques. Furthermore, one can identify approaches to consider the entire system of equations in a complete multigrid framework, such as the approach presented by Shyy and Sun³³ and Shyy.³⁴ The cost of this step is possibly one of the most demanding and hence needs to be performed as less frequently as pos-

TABLE II. Summary of boundary conditions for the different variables.

Variable	Open boundary	Electrode/dielectric surface
ϕ -potential	Zero gradient	At the submerged electrode: $\phi=0$ At the exposed electrode: $\phi=\phi_0 \sin(2\pi ft)$, $\phi_0=1$ kV
Electron, ion species	Zero gradient	Electrode: Electrons: Away from the electrode: flux=0 If drift is toward the electrode: flux= $n_e v_{eth}$, where v_{eth} is the thermal velocity. Ions: Away from the electrode: flux=0 If drift is toward the electrode: zero gradient On the dielectric Allow surface charge accumulation. To do this the current continuity is established, i.e., at the dielectric-gas interface the species flux is determined by $\frac{\partial(\epsilon_{\text{gas}} E_{\text{gas}})}{\partial t} + \frac{e}{\epsilon_0} (n_i v_i - n_e v_e)_{\text{gas}} = - \frac{\partial(\epsilon_{\text{dielectric}} E_{\text{dielectric}})}{\partial t}$

sible. The choice of the global time step for integrating the system is determined taking this into account.

It is noted that for the low-speed, i.e., incompressible, fluid flow applications, which is the current focus, the fluid characteristic time scales are much larger than that of the operating plasma dynamics. For example, for an airfoil of 15 cm chord, at the Reynolds number of 10^4 , the convective time scale is $O(10^{-1}$ s) if one considers air as the fluid. In comparison, for a DBD device at 10 kHz, the period is $O(10^{-4}$ s). While the plasma dynamics time scales are important, it has been shown in our earlier work³² that they are much smaller [$O(10^{-7}$ s) than the the ion convection regime] for the operating conditions of interest. Hence, we can safely treat the coupling between the fluid and plasma physics as one way, i.e., from the plasma to the fluid by means of the body force model. The instantaneous body force is calculated here as the locally generated Lorentz force given by the product of the net charge and the electric field strength. To extend further, if the fluid dynamic time scales become com-

parable, then the two-way coupling will need to be handled and the fluid solution advancement should be performed using the DBD time scale.

III. RESULTS AND DISCUSSION

In this section, we will model the two-dimensional radio frequency DBD in helium gas at high pressure in an asymmetric configuration, as shown in Fig. 2. The electrodes are 2 mm in length and the insulated bottom electrode is shifted downstream by 2 mm. Roy and co-workers¹⁷⁻²¹ have studied a similar case. The helium discharge is modeled at a pressure of 300 torr and a temperature of 300 K and is driven by an ac voltage of 1 kV (peak value of sinusoidal voltage) unless specified otherwise. The frequency is varied in the range of 5–20 kHz and is specified as relevant. The thickness of the electrodes is negligible and the dielectric thickness is 5 mm. The electron temperature is assumed to be 1 eV ($\sim 11\,600$ K), while the ions and the neutrals are essentially in thermal equilibrium at 300 K.

The computational domain employed is a square domain of size of $1 \times 1 \times 1$ cm³ (unit cm in the spanwise direction). The grid consists of 127×61 points for the 2D case, as shown in Fig. 2(b). The dielectric constant in the fluid/discharge domain is 1.0055; the permittivity of vacuum and that of the insulator is varied between 1 and 30. For investigation purposes, the frequency is varied from 5 to 30 kHz, with all other conditions remaining constant. A global integration time step of 10^{-8} s is used for the computations. The initial number density in the plasma is $10^9/\text{cm}^3$ for all the different species.

The various transport properties and property relationships are available in literature and we will use the ones used by Singh *et al.*¹⁷ for the present study. These are summarized in Table I. It should be noted that the transport properties are written as a function of the pressure (p): in the present study, it is based on Torr.

Boundary conditions. The boundary conditions are sche-

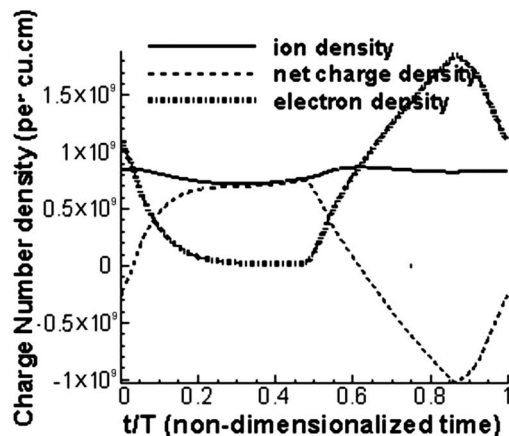
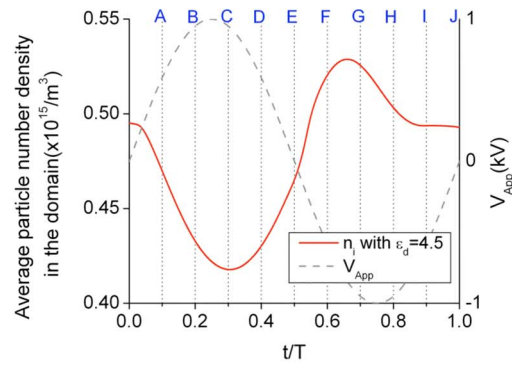
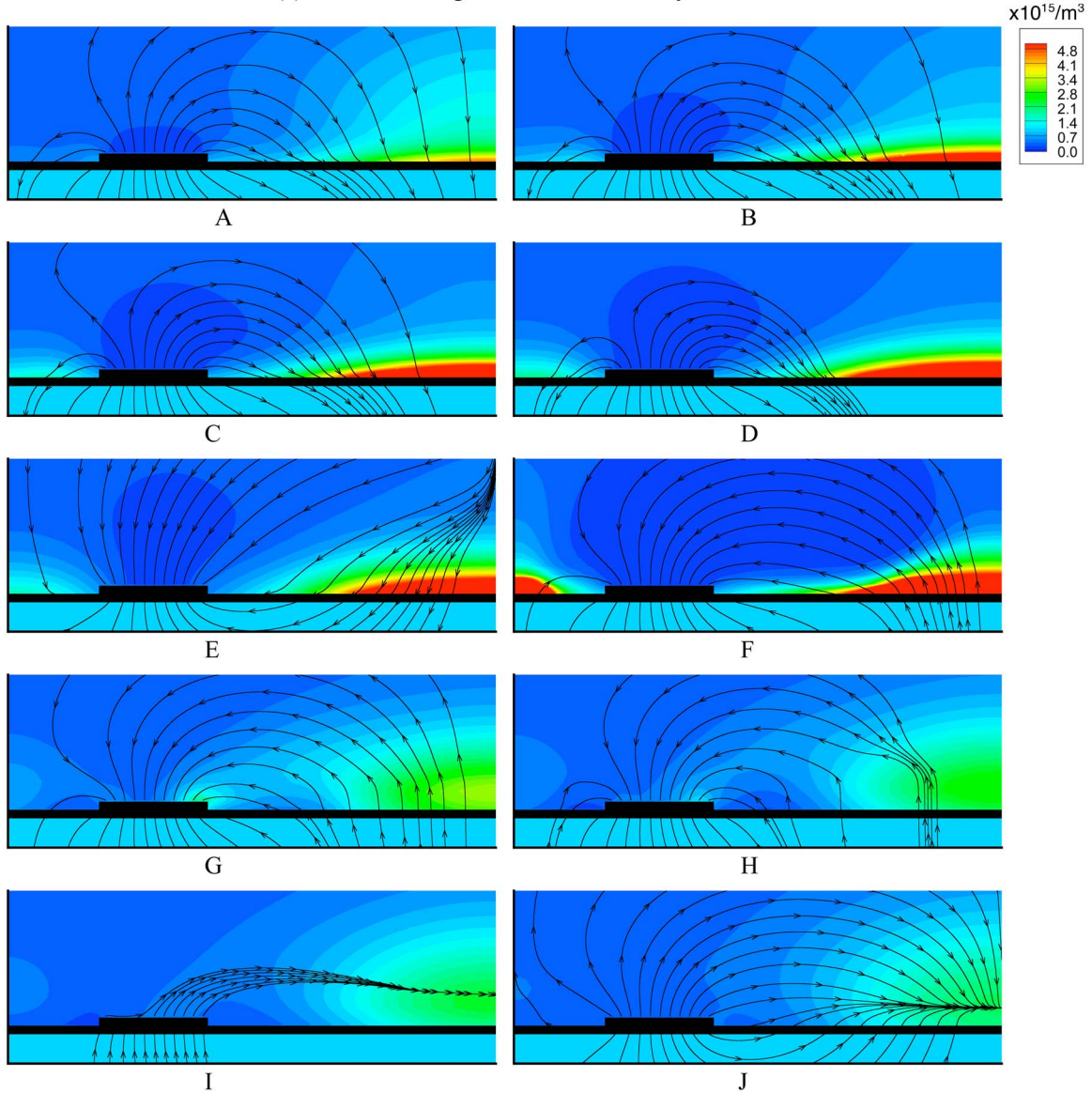


FIG. 3. Time dependent plasma behavior for one time cycle (5 kHz, 1 kV applied voltage). Domain-averaged species charge density and net charge density variation are shown.



(a) Domain-averaged ion number density over time.



(b) Instantaneous snapshots of the ion density at different instants over a cycle.

FIG. 4. (Color online) Ion density (contour) evolution in the domain over one time cycle (5 kHz, 1 kV applied voltage). The electric field vectors are shown to indicate instantaneous ion drift.

matically presented in Fig. 2(b). The homogeneous Neumann boundary condition is applied for the electrostatic potential (Φ) at the open boundaries, while the Dirichlet boundary condition is used at the electrode: At the exposed electrode:

$\phi = \phi_0 \sin(2\pi ft)$, where ϕ_0 is the peak value. At the submerged electrode: $\phi = 0$.

A harmonic voltage of (frequency f) is used as the base waveform. For the plasma species modeling, the domain

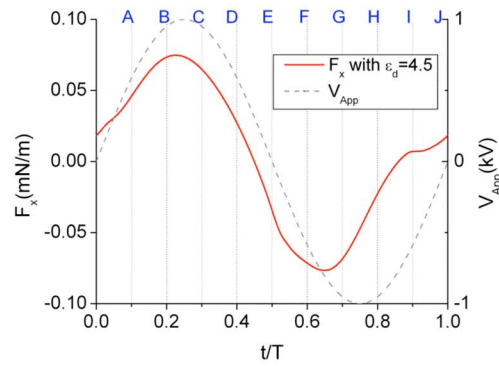
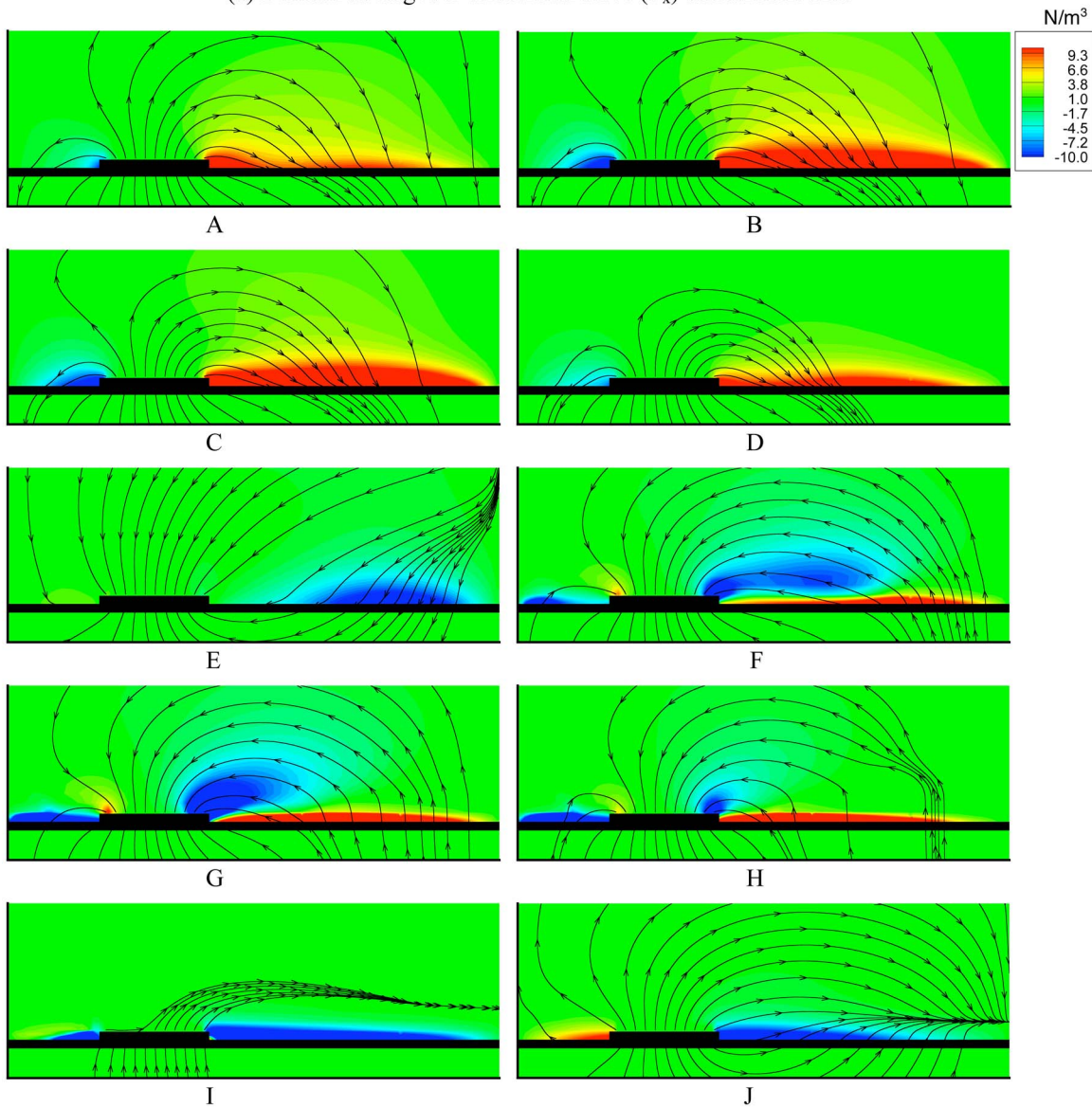
(a) Domain averaged x-directional force (F_x) variation in time(b) Instantaneous snapshots of the F_x field at different instants over a cycle.

FIG. 5. (Color online) Force evolution over one time cycle (5 kHz, 1 kV applied voltage). Part b shows the force contours superimposed with the instantaneous electric field vectors.

boundary away from the insulator/electrode surface is assigned a zero normal gradient condition assuming insignificant impact far away from the fluid-actuator interface. At the dielectric surface, the drift current and the displacement current from the gas domain is balanced with the displacement

current inside the insulator. At the electrode, the treatment is slightly different. The electrons are assumed to be isothermal (at 11 600 K or 1 eV) at boundaries. At the exposed electrode, the thermal flux toward the wall is considered while it is neglected when the drift is away from the wall. For the

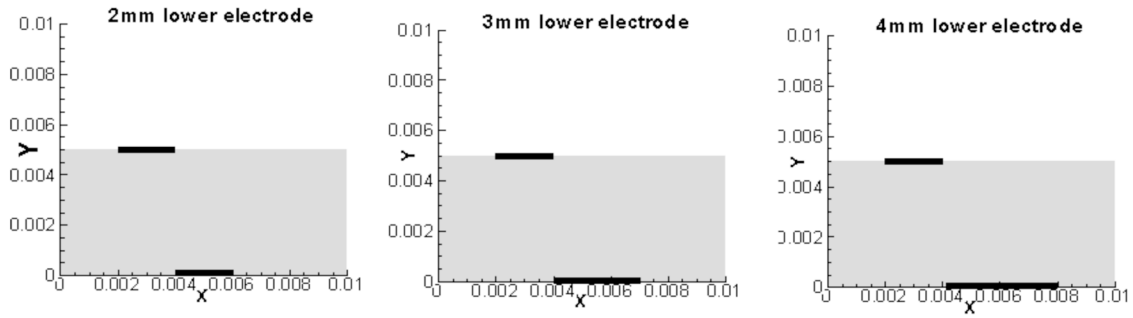


FIG. 6. (Color online) Three different lower electrode lengths modeled to investigate the effect of increased surface area on the discharge.

ions or the heavier species, the drift effects are significant and hence a zero gradient (normal to the boundary) condition ($\partial n_{i,e}/\partial n=0$) is applied. The boundary conditions are summarized in Table II.

Plasma species initial condition. The initial condition used to start the simulation requires specifying the starting number densities for the various species. Ideally, the simulation should start from a very small charge concentration, but to accelerate the evolution of the transient behavior to a periodic steady state solution, we will use a weakly preionized neutral gas with an initial charge concentration of $10^9/\text{cm}^3$. Our simulations reveal that the dynamics of the operating discharge plasma actuator is more a function of the difference in the values of $(n_i - n_e)$ or more generally the net charge in the region. It is observed that the periodic steady state solution is attained much quicker with a starting guess of $10^9/\text{cm}^3$ and is used as the initial condition for the results presented here.

A. Plasma structure

In the following discussion, we will analyze the discharge structure evolution in space and time for helium gas, generated in an asymmetric configuration, as described in Fig. 2. The numerical simulation shown is for 1 kV and 5 kHz applied sinusoidal voltage waveform.

Self-limiting discharge. It is common knowledge that the breakdown is quenched and controlled by the accumulated

charge since the discharge terminates on a dielectric surface, resulting in the self-limiting nature of the discharge. This can be observed from the experimental observations⁶ where a continuously varying applied voltage is necessary to sustain the discharge. In that study, the light intensity observed is zero as soon as the observed potential reaches either maxima or minima. It should be noted here that the experimental study is based on the light emission from the excited metastables and hence a direct comparison with the numerical results is not presently possible. Recently, Font *et al.*²⁹ observed accumulation of negative voltage over the dielectric surface from experiments and Roy *et al.*³⁵ numerically predicted electron accumulation downstream of the exposed electrode. Both studies qualitatively support the results from the present work.

Figure 3 shows the mean density variation in time for the different species and the net charge density for a sinusoidal voltage variation. It is known that in the positive half-cycle, the ions move away from the electrode and tend to get deposited on the insulator surface. Hence, the decrease in the average ion density over the domain as the averaging process does not account for the surface deposition. Similar to the experimental observation, this decrease in ion density is stopped when the increase in voltage is zero near the maxima. This can be clearly seen in the evolution of the ion density in the domain, as shown in Fig. 4.

Specifically in the first quarter of the actuator cycle as can be seen in instants A, B, and C, the ion concentration increases near the dielectric surface and the free concentration in the domain at its minimum. At instants D, E, and F, the applied voltage starts decreasing, causing the built-up potential from the accumulation to dominate resulting in releasing the ion species into the bulk region. The ion density reaches its maximum value between instants F and G. At this point, the change in polarity enhances the release of ions which travel toward the negative exposed electrode. However, there is no ion buildup during this part of the cycle as the electrode being a conductor absorbs the incoming charge

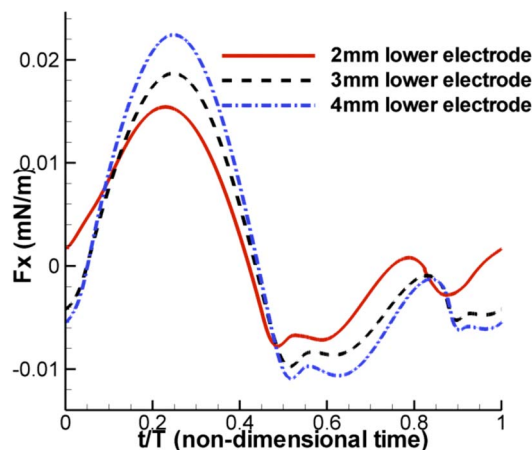


FIG. 7. (Color online) Impact of lower electrode size (20 kHz, 400 V applied voltage).

TABLE III. Force dependence on the lower electrode size.

Lower electrode size (mm)	$F_{x,av}$ (mN/m)
2	0.00023
3	0.00065
4	0.0010

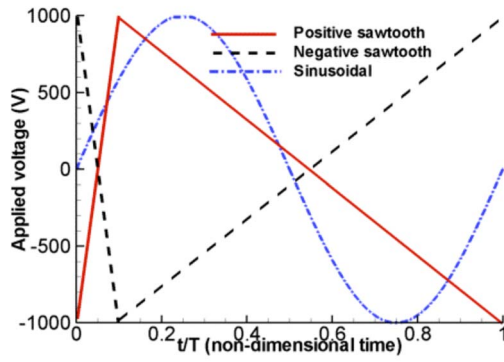


FIG. 8. (Color online) Different input asymmetric sawtooth voltage signals (1 kV, 10 kHz) used in the numerical study.

flux. Before instant I, Fig. 4(a) shows the ion number density as stabilizing due to the equilibrium attained between the absorption at the electrode, the accumulated ion release from the insulator surface, and the ionization/recombination phenomena in the bulk region. This behavior continues for the rest of the cycle.

Force variation. The domain averaged force variation in time presented in Fig. 5(a) shows that the positive half-cycle has a predominantly positive force, while the negative half-cycle has both positive and negative components. This is clearly seen from the evolution of the force field over time, as shown in Fig. 5(b). It is well known that the bulk of the momentum transfer is achieved by the heavier ion species in the domain. As can be seen from Fig. 4(b), the positive half-cycle corresponding to instants A, B, C, D, and E correspond to the accumulation of ion species on the insulator surface from the bulk of the domain. Since the submerged electrode is downstream, the bulk of the transport in this half is in the positive direction and to a lesser extent in the negative direction. Hence, the strong positive force regions near the insulator surface downstream of the electrode and a weaker component upstream of the electrode for instants A, B, C, and D, as seen in Fig. 5(b). Starting from instant E at which time the charge buildup reverses the polarity of the potential in the region. This happens for a half-cycle corresponding to instants E and F during which the weak negative force region near the downstream insulator surface exits due to the ion

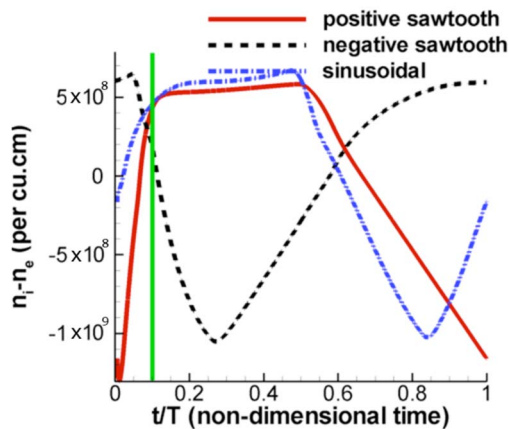


FIG. 9. (Color online) Impact of waveform on the net species charge number density.

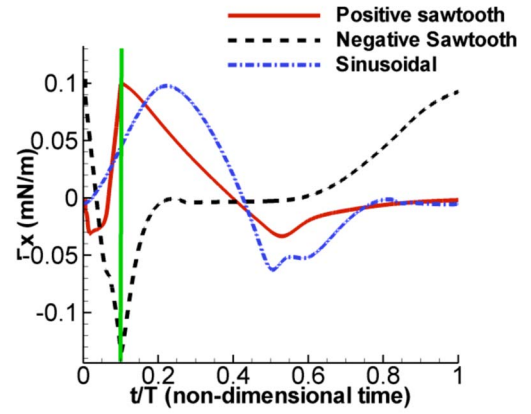


FIG. 10. (Color online) Domain averaged F_x with time for different waveforms (10 kHz, 1 kV applied voltage). The green vertical line indicates the instant of change in slope in the sawtooth waveform.

transport toward the upstream electrode. An interesting phenomenon happens at this instant in the cycle. It should be noted that during this half-cycle, the electrons are the species which get accumulated on the dielectric surface resulting in the charge buildup. However, the electrons being lighter species travel faster and hence the faster charge buildup and a quicker reversal of polarity in the domain occur.

There is a qualitative similarity between the instants G, H, I and B, C, D in Fig. 5(b), but the process is faster. The above mechanism renders the force weaker in this negative half, as the discharge is quenched early. This force generation efficiency throughout one cycle is of importance here as the slower response time of the fluid will only see the net overall force generation over a few time cycles and is less sensitive to the fluctuation over time.

Asymmetry in the discharge. The above discussion on the time evolution of the force field indicates two different processes in the two half-cycles. The first half-cycle shows a pure ionization and deposition of the slower ion species on the insulator surface, while the second half-cycle shows the faster deposition of electrons with the same mechanism. This difference in the mobilities of the two species and the geometric asymmetry affects the discharge evolution in the second half-cycle. This asymmetry can be observed in the experimental measurements⁶ as well.

B. Geometric effects

Impact of lower electrode size. Here, we fix the length of the top electrode and vary the bottom electrode to gauge the impact of the area covered by the net surface discharge formation (Fig. 6). The actuator operates with a 20 kHz, 400 V sinusoidal voltage waveform. Figure 7 and Table III indicate that the weakest force field is obtained for the 2 mm

TABLE IV. Domain averaged force over the voltage cycle for different waveforms

Waveform	$F_{x,av}$ (mN/m)
Positive sawtooth	0.0068
Negative sawtooth	0.0063
Sinusoidal	0.0081

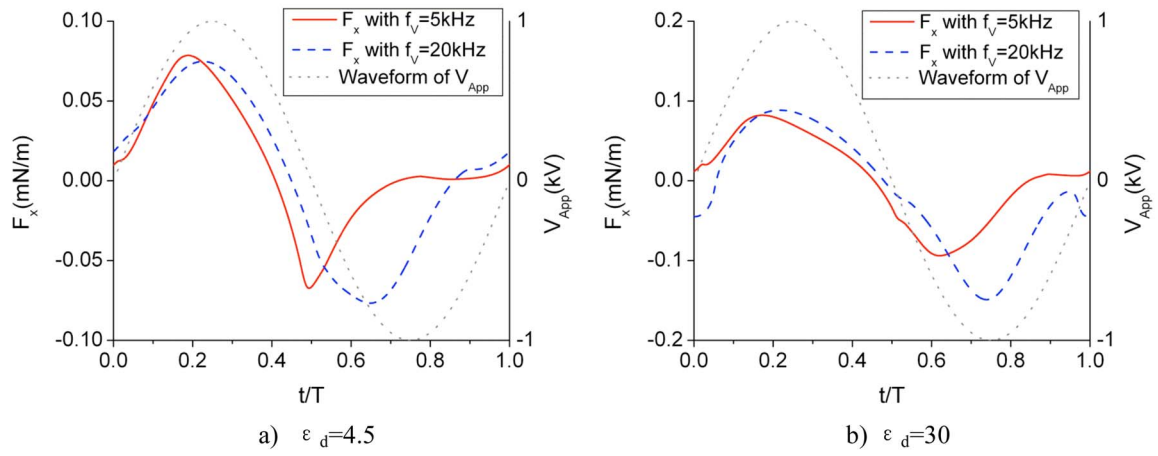


FIG. 11. (Color online) Frequency effect for different dielectric constants.

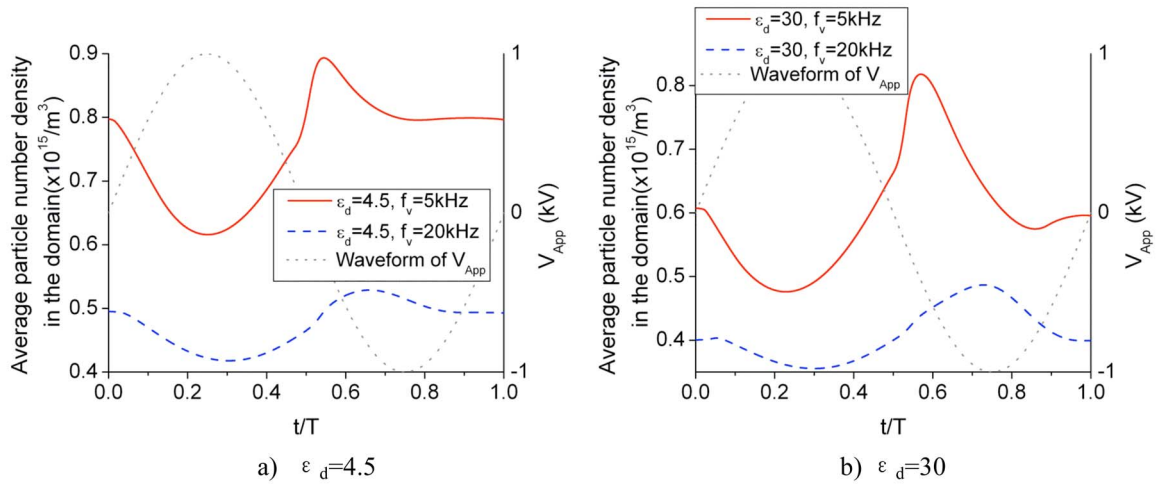


FIG. 12. (Color online) Domain averaged ion number density.

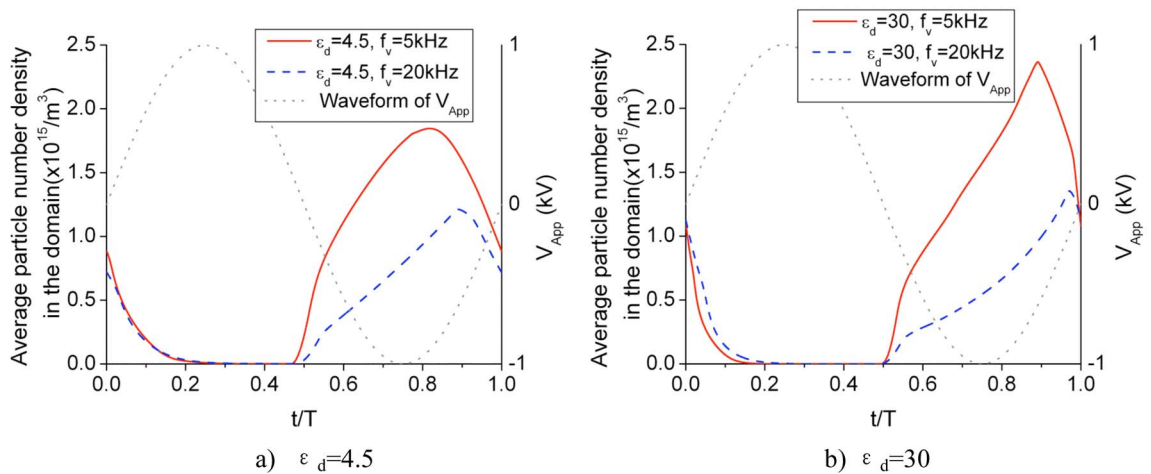


FIG. 13. (Color online) Domain averaged electron number density.

TABLE V. Domain averaged force over the voltage cycle for different frequencies.

Frequency (kHz)	$F_{x,av}$ (mN/m)
20	0.0059
10	0.0095
5	0.0125

electrode case, while there is steady increase in the net force value as the size of the bottom electrode increases. This effect is because the larger lower electrode obviously results in a much larger surface discharge generation and hence the stronger force field. However, once the lower electrode becomes sufficiently large, a balance between size and strength will be reached signifying the most efficient configuration. Similar trends have been observed by experimental studies such as by Enloe *et al.*⁶

C. Effects of applied voltage

Impact of waveform. The observed behavior for the harmonic waveform indicated that the positive going half (irregular) had a different discharge characteristic as compared to the negative going half (uniform discharge) leading to the asymmetry which causes the unidirectional momentum coupling with the fluid flow. Enloe *et al.*⁶ measured the thrust produced by the actuator for two different sawtooth waveforms (positive and negative, as shown in Fig. 8) using a mass balance to assess efficiency of the two half-cycles. The positive sawtooth has a faster varying positive going voltage and a slower varying negative going voltage and vice versa for the negative sawtooth. The result⁶ clearly showed that the positive sawtooth is more efficient compared to the negative sawtooth waveform. This is because unlike the light intensity measurements, the force orientation tends to depend heavily on the geometric asymmetry and hence strongly dependent on the polarity of the exposed and the submerged electrodes. On the other hand, the magnitude of the force is a function of the strength of the discharge and charge concentration available in the domain. The positive sawtooth has a stronger positive going part which results in a strong breakdown,

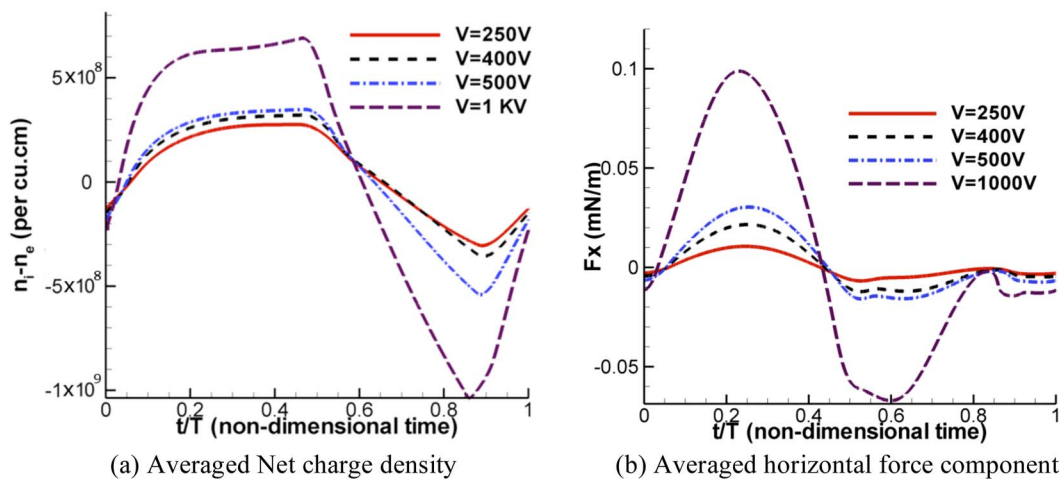
TABLE VI. Mean domain averaged force over the time cycle for different voltages.

Voltage (V)	$F_{x,av}$ (mN/m)
250	0.0008
400	0.0017
500	0.0026
1000	0.006

while the negative sawtooth has a stronger negative going part. Figure 9 compares the domain-averaged net charge number density for the two different waveforms. One can infer from the force response to the harmonic waveform [Fig. 5(a)] that the positive going part (exposed electrode is positive) is possibly more efficient than the negative going part. The domain-averaged force responses for the sawtooth waveforms (1 kV, 10 kHz) are shown in Fig. 10. The force for the positive and negative sawtooth waveforms starts the time cycle in the similar fashion with negative slope. For the negative sawtooth, the force continues on its negative slope and attains a negative peak during the fast varying early phase (negative-going voltage) and then steadily increases to a positive value during the slow-varying positive-going phase. The harmonic waveform seems to be the most efficient waveform. The negative sawtooth is the least efficient with the positive sawtooth falling in between. The force profile over time indicates that the positive going phase is the most efficient part of the voltage cycle for the asymmetric actuator modeled in this study (see Table IV).

Impact of frequency. The effect of frequency with different dielectric constant is presented in Fig. 11. The increase in the frequency of applied voltage basically induces the increase and delay in the negative force generation which significantly decreases the time-averaged force generation even to the negative sign.

In general, the increased frequency induces lower amount of charged particles since the time in which the electric field is sufficient enough to ionize particles is shorter, which means less ionization, as in Fig. 12. For the same reason, the case with lower frequency shows faster electron

FIG. 14. (Color online) Charge density and force variation over time for different voltages (20 kHz of frequency, $\epsilon_d=4.5$).

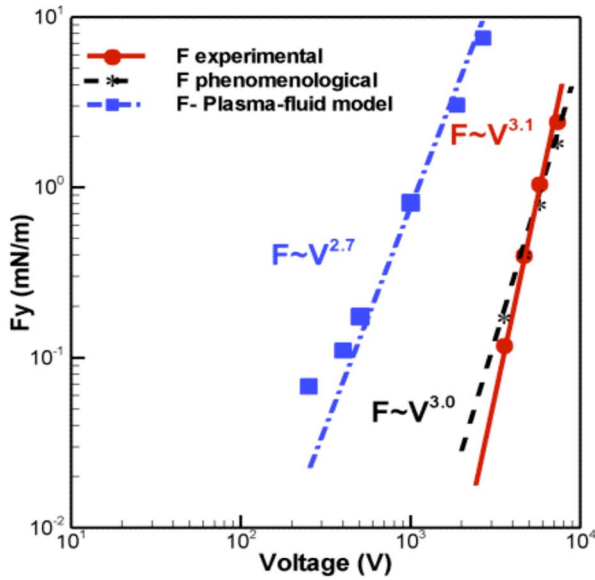


FIG. 15. (Color online) $F_{y,av}$ power-law dependence on voltage is compared for two different numerical models—phenomenological and the first-principles-based plasma fluid model (20 kHz) along with experimental data of Ref. 13. The arrows point to the set of axes chosen for each of the curves.

accumulation on the surface in the normalized time coordinate which results in the faster saturation, as in Fig. 13, although the actual growth rate of electron numbers in the case of higher frequency is similar to or higher than the lower one differently from the normalized time result. The time-varying pseudoelectrode which is the region of the accumulated electrons is affected by the number of accumulated electrons at each time and can significantly affect the electric field for the following half-cycle when their accumulation is prominent.

Comparing Fig. 11 with Fig. 13, it is evident that the saturation of electron accumulation is responsible for the restriction of negative force generation. However, if the saturation is allowed to happen nearly at the end of the second cycle as $f_v = 20$ kHz in Fig. 13(b), a drop in F_x before the next positive cycle may occur as in Fig. 11(b), which also contributes to bias the average force to decrease. With the increased frequency of the applied voltage, this pseudoelectrode with negative charge remains weaker, compensates less of the electric field near the surface compared to the lower frequency, and as a result produces higher magnitude of the negative force in the second half cycle. As a result, increased frequency results in decrease in time and domain averaged force $F_{x,av}$ as in Table V.

Impact of voltage magnitude. The net charge density and F_x history are presented in Fig. 14 and $F_{x,av}$ in Table VI with various magnitude of applied voltage (20 kHz frequency) ranging from 250 to 1000 V. The force shows a power-law dependence on the applied voltage. In Fig. 15, three different force measurements are compared for their voltage dependence. The experimental (work of Van Dyken *et al.*¹³) and the phenomenological model data are the same used in our earlier study⁸ and use air as the modeling fluid. In order to compare with the experiments, the normal force (y) acting on the actuator surface is used for establishing the correlation as against the axial components (x) employed so far. It can be

TABLE VII. Dielectric constant of materials (at 25 °C, 10 kHz).

Material	Air	Plasticell ^a (polyvinyl chloride)	Glass-epoxy ^b	Alumina	Thallium bromide ^a	Barium titanite
Dielectric constant	1.000 54	1.04	5.2	10	30.3	1200

^aReference 36.

^bReference 37.

seen that phenomenological and the experimental measurements have one common data point which is employed to close the model. The remaining data points are predicted with reasonable accuracy by the linear field or phenomenological approach with a voltage (V) dependence of $V^{3.0}$ as against the $V^{3.1}$ dependence from the experiment.¹³ The first-principles/hydrodynamic plasma model for Helium shows a $V^{2.7}$ power-law for the force generation. The difference can be attributed to the different species dynamics between the helium and air chemistry as well as the choice of voltage regime employed. Overall, it is worth noting that this power-law behavior is desirable for enhancing the actuator operating range. It is noted that the x -component of the force has a similar dependency on the applied potential as the y -component by virtue of its definition. Specifically, the force components are calculated as the product of the local charge and the local field ($-d\Phi/dx$ or $-d\Phi/dy$) and one would expect the x - and y -components of the field to have a similar behavior with varying potential (Φ).

D. Effect of material property (dielectric constant)

To investigate the effect of the dielectric constant on force generation, several cases are modeled. Some materials used in the various studies are presented in Table VII. In this study, the dielectric constant is varied as 1, 4.5, and 30, which may not have corresponding materials but convey some insights of the effect of the constant. The voltage source used is a harmonic waveform of 1 kV and 20 kHz frequency.

There are some diverse features observed with different dielectric constants. In Fig. 16(a), there is higher concentration of negative force at $t/T = 0.7$ for $\epsilon_d = 30$, which is absent for $\epsilon_d = 1.0$. This is related to the deformation of the electric field line, increased near-wall electric field strength (which will be shown later), and the difference in the resulting charged particle movement. Figure 16(b) shows the force contours with the instantaneous electric field line vectors.

From the electron and ion number density contours of Figs. 17(a) and 17(b), it can be seen that the concentration of ions near the upper electrode is prominent for higher ϵ_d which corresponds to the same region as the minimum negative force during the second half-cycle. Though the accumulation of electrons on the dielectric surface continues the second half-cycle, there is a point of time at which the accumulated electron layer reaches the upper electrode and those accumulated particles create a pseudoelectrode on the surface with significant change in the electric field.

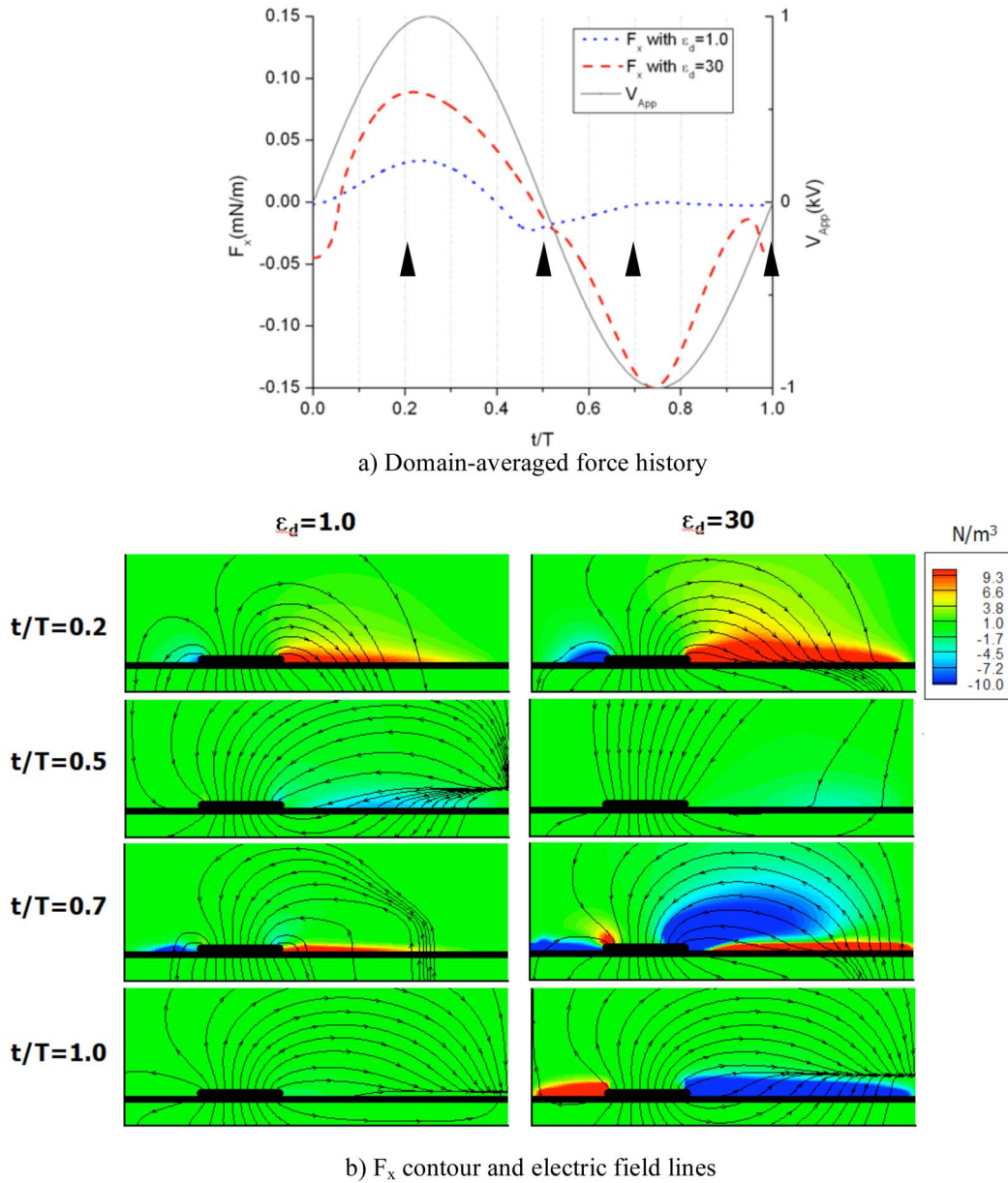


FIG. 16. (Color online) Effect of dielectric constant (20 kHz, 1 kV): force evolution. Here, the force contours are shown along with the instantaneous electric field vectors.

Figure 18 shows the x -directional electric field strength E_x along the surface which starts from the right end of the upper electrode for the two different materials. The comparison of the two cases indicate that the higher dielectric constant results in a higher value and steeper slope for E_x . The higher the constant means increase in the polarization tendency of the material and thus decreased electric potential near the wall. This behavior for higher dielectric constant causes lower potential on the dielectric surface apart from the upper electrode and higher strength and steeper slope in electric field, especially E_x near the wall as a result. This effect is prominent when the applied voltage reaches the positive and negative peaks at which the effect of charged particles on the electric field is weak. The magnitude of E_x is closely related to the generation of charged particles as well as instantaneous force generation. The higher peak value

near the electrode ($x=0$) at $t/T=0.7$ in the case of $\epsilon_d=30$ explains the distinctive ion generation in this region mentioned above. In Fig. 18(b), the flat part of $\epsilon_d=30$ case at $t/T=0.7$ which starts from $x=0.0042$ to the end of the domain corresponds to the length of the electron layer spread at that time which eliminates the electric potential difference in the region. This effect does not exist explicitly for the ion accumulation which prevails during the former half-cycle.

IV. CONCLUSIONS

A hydrodynamics plasma model in the context of a discharge-induced thermofluid transport is presented. This provides a way of self-consistent modeling of the discharge effects as opposed to an analytical-empirical model previously developed.¹ The two-dimensional helium dielectric

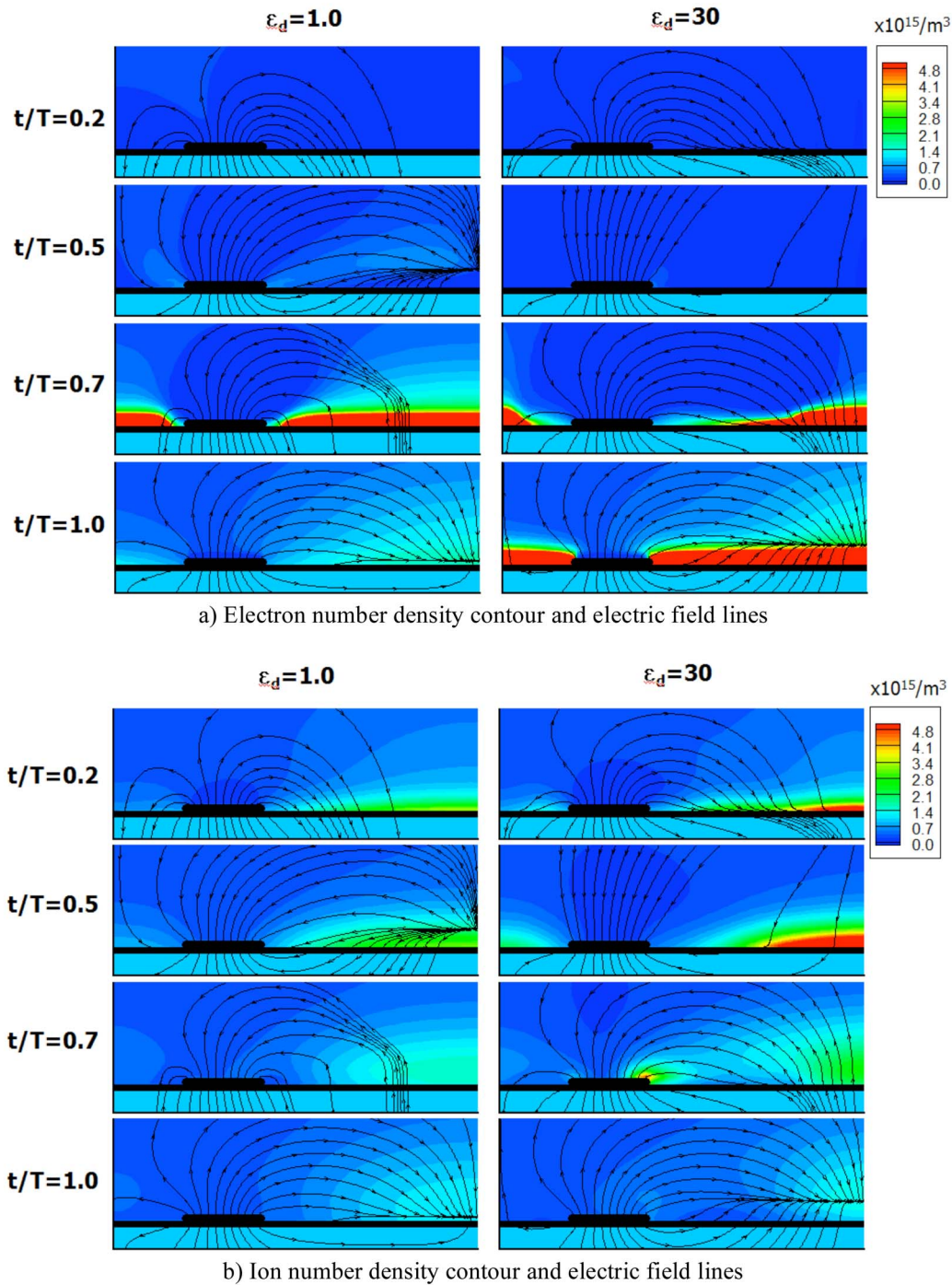


FIG. 17. (Color online) Effect of dielectric constant (20 kHz, 1 kV): species evolution. Here, the force contours are shown along with the instantaneous electric field vectors.

barrier discharge in an asymmetric geometry has been modeled using a finite volume operator-split sequential approach to efficiently solve the multiscale problem. The two-species plasma simulations revealed that the generation of the unidirectional momentum coupling is primarily affected by the combination of factors such as the asymmetry of the geometric arrangement, the waveform of the applied voltage, the species mobility, and dielectric material.

Overall characteristics of the plasma dynamics. There are two different processes in the two half-cycles of the ac-

tuator operation, largely due to the difference in mobility between faster electrons and slower ions, and the geometric configurations of the insulator and electrodes. The first half-cycle is characterized by the deposition of the slower ion species on the insulator surface while the second half-cycle by the deposition of the electrons at a faster rate. Regarding the various actuator parameters, the following observations can be summarized.

Impact of lower electrode size. The increased lower electrode size provides the larger area available for the deposi-

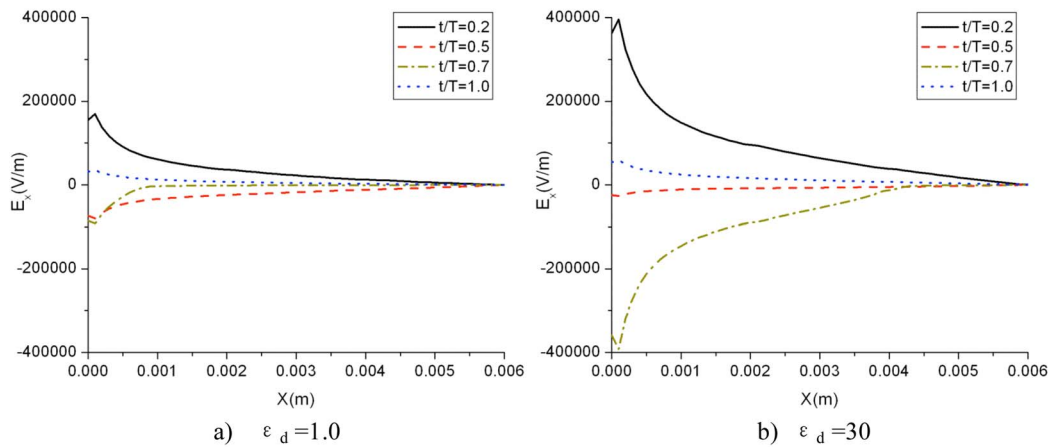


FIG. 18. (Color online) E_x along the dielectric surface (20 kHz, 1 kV).

tion of charged particles which also results in the increase of the peak values of the time-varying force.

Impact of waveform. Introducing positive and negative sawtooth waveforms affects the rate of change in particle number densities and force history, but it does not increase the resultant average force. Specifically, the study indicates that the rate of applied voltage variation and the duration of the polarity, both play a role in the net force generation.

Impact of voltage. The sensitivity of the generated force to the magnitude of the applied voltage for a sinusoidal (symmetric) waveform shows a near cubic (~ 2.7) dependence for the first-principles hydrodynamic model in helium gas. This is in the region of the observed experimental dependency for air which is ~ 3.1 and the phenomenological model (~ 3.0).

Impact of frequency. The frequency of the applied voltage interplays with physical length scales—electrode size and spacing of the actuator and the mobility of each particle species, determining the time allowed for particles to deposit on or release from the dielectric surface. This especially affects the polarity reversal phases in each cycle, resulting in the increased asymmetry of waveform and averaged force with the lower frequency.

Effect of material property—dielectric constant. The change in the dielectric constant of the insulator mainly affects the electric field near its surface which determines the degree of ionization and deposition of charged particles. Although the increased dielectric constant produces higher peaks in each half-cycle of time-varying force, the resultant average force decreases mainly due to the decrease in overall asymmetry of the waveform.

The effect of frequency is found to be modest as compared to the sensitivity to the applied voltage which shows a power-law dependence on the voltage for the measured force in the domain. This relationship shows substantial similarity to the experimental measurements and the phenomenological model. The strong power-law dependence of the force on the voltage is attractive for generating huge momentum fluctuations with smaller voltage variation requirements.

It seems that there are two conditions to obtain higher axial force which is delivered to the neutral fluid—increasing

the peak value of the cyclic force generation and introducing more asymmetry to the first and second half of the cycle to make the positive part more prominent. Although various parameters are coupled and correlated to each other, the increase in the lower electrode size, applied voltage, and dielectric constant tend to contribute to the first factor, and the decrease in frequency of applied voltage tend to contribute to the second factor. To generate higher force, these parameters including others need to be adequately tuned to accomplish those conditions.

ACKNOWLEDGMENTS

The present work has been supported in part by the Air Force Research Laboratory, Flight Vehicle Directory, under the Collaborative Center in Aeronautical Science project, Dr. Jack Benek program monitor.

- ¹W. Shyy, B. Jayaraman, and A. Anderson, *J. Appl. Phys.* **92**, 6434 (2002).
- ²J. R. Roth, D. M. Sherman, and S. P. Wilkinson, 36th AIAA Aerospace Sciences Meeting and Exhibit, Reno, NV, 1998 (unpublished), Paper No. AIAA-1998-0328.
- ³T. C. Corke and E. Matlis, Fluids 2000, Denver, CO, 2000 (unpublished), AIAA Paper No. 2000-2323.
- ⁴M. L. Post and T. C. Corke, 41st Aerospace Sciences Meet and Exhibit, Reno, NV, 2003 (unpublished), AIAA Paper No. 2003-1024.
- ⁵T. C. Corke, E. J. Jumper, M. L. Post, D. Orlov, and T. E. McLaughlin, 41st Aerospace Sciences Meeting and Exhibit, Reno, NV, 2003 (unpublished), AIAA Paper No. 2002-0350.
- ⁶C. L. Enloe, T. E. McLaughlin, R. Van Dyken, and K. D. Kachner, *AIAA J.* **42**, 589 (2004).
- ⁷F. O. Thomas, A. Kozlov, and T. C. Corke, 11th AIAA/CEAS Aeroacoustics Conference (26th AIAA Aeroacoustics Conference), Monterey, California, 2005 (unpublished), AIAA Paper No. 2005-3010.
- ⁸B. Jayaraman and W. Shyy, 33rd AIAA Fluid Dynamics Conference and Exhibit, Orlando, 2003 (unpublished), AIAA Paper No. 2003-3712.
- ⁹J. Poggie, 37th AIAA Plasmadynamics and Lasers Conference, San Francisco, CA, 2006 (unpublished), AIAA Paper No. 2006-3567.
- ¹⁰J. Poggie, 44th Aerospace Sciences Meeting and Exhibit, Reno, NV, 2006 (unpublished), AIAA Paper No. 2006-1007.
- ¹¹J. R. Roth, R. C. M. Madhan, M. Yadav, J. Rahel, and S. P. Wilkinson, 42nd AIAA Aerospace Sciences Meeting and Exhibit, Reno, NV, 2004 (unpublished), AIAA Paper No. 2004-845.
- ¹²T. C. Corke and M. L. Post, 43rd Aerospace Sciences Meeting and Exhibit, Reno, NV, 2005 (unpublished), AIAA Paper No. 2005-0563.
- ¹³R. Van Dyken, T. E. McLaughlin, and C. L. Enloe, 42nd Aerospace Sci-

- ences Meet and Exhibit, Reno, NV, 2004 (unpublished), AIAA Paper No. 2004-846.
- ¹⁴J. R. Roth and X. Dai, 44th Aerospace Sciences Meeting and Exhibit, Reno, NV, 2006 (unpublished), AIAA Paper No. 2006-1203.
 - ¹⁵J. Pons, E. Moreau, and G. Touchard, *J. Phys. D* **38**, 3635 (2005).
 - ¹⁶B. Jayaraman, S. Thakur, and W. Shyy, 44th Aerospace Sciences Meeting and Exhibit, Reno, NV, 2006 (unpublished), AIAA Paper No. 2006-0686.
 - ¹⁷K. P. Singh, S. Roy, and D. V. Gaitonde, 37th AIAA Plasmadynamics and Lasers Conference, San Francisco, CA, 2006 (unpublished), AIAA Paper No. 2006-3381.
 - ¹⁸S. Roy, K. P. Singh, H. Kumar, D. V. Gaitonde, and M. Visbal, 44th Aerospace Sciences Meeting and Exhibit, Reno, NV, 2006 (unpublished), AIAA Paper No. 2006-374.
 - ¹⁹S. Roy and D. V. Gaitonde, 43rd AIAA Aerospace Sciences Meeting and Exhibit, Reno, NV, 2005 (unpublished), AIAA Paper No. 2005-0160.
 - ²⁰S. Roy and D. V. Gaitonde, 35th AIAA Fluid Dynamics Conference, Toronto, Canada, 2005 (unpublished), AIAA Paper No. 2005-4631.
 - ²¹K. P. Singh and S. Roy, *J. Appl. Phys.* **98**, 083303 (2005).
 - ²²D. V. Gaitonde, M. R. Visbal, and S. Roy, 36th Plasmadynamics and Lasers Conference, Toronto, 2005 (unpublished), AIAA Paper No. 2005-5302.
 - ²³K. P. Singh, S. Roy, and D. V. Gaitonde, *Plasma Sources Sci. Technol.* **15**, 735 (2006).
 - ²⁴J. P. Boeuf, Y. Lagmich, Th. Callegari, and L. C. Pitchford, 45th Aerospace Sciences Meeting and Exhibit, Reno, NV, 2007 (unpublished), AIAA Paper No. 2007-183.
 - ²⁵K. P. Singh and S. Roy, *J. Appl. Phys.* **101**, 123308 (2007).
 - ²⁶A. V. Likhanskii, M. N. Shneider, S. O. Macheret, and R. B. Miles, 44th Aerospace Sciences Meeting and Exhibit, Reno, NV, 2006 (unpublished), AIAA Paper No. 2006-1204.
 - ²⁷A. V. Likhanskii, M. N. Shneider, S. O. Macheret, and R. B. Miles, 45th Aerospace Sciences Meeting and Exhibit, Reno, NV, 2007 (unpublished), AIAA Paper No. 2007-673.
 - ²⁸A. V. Likhanskii, M. N. Shneider, S. O. Macheret, and R. B. Miles, 45th Aerospace Sciences Meeting and Exhibit, Reno, NV, 2007 (unpublished), AIAA Paper No. 2007-4533.
 - ²⁹G. I. Font, C. L. Enloe, T. E. McLaughlin, and D. Orlov, 45th Aerospace Sciences Meeting and Exhibit, Reno, NV, 2007 (unpublished), AIAA Paper No. 2007-188.
 - ³⁰P. Colella, M. R. Dorr, and D. D. Wake, *J. Comput. Phys.* **152**, 550 (1999).
 - ³¹B. Jayaraman and W. Shyy, *Prog. Aerosp. Sci.* **44** (2008).
 - ³²B. Jayaraman, S. Thakur, and W. Shyy, *J. Heat Transfer* **129**, 517 (2007).
 - ³³W. Shyy and C.-S. Sun, *Comput. Fluids* **22**, 51 (1993).
 - ³⁴W. Shyy, *Computational Modeling for Fluid Flow and Interfacial Transport* (Elsevier, Amsterdam, 1994).
 - ³⁵S. Roy, *Appl. Phys. Lett.* **86**, 101502 (2005).
 - ³⁶A. R. Von Hippel, *Dielectric Materials and Applications* (The Technology Press of MIT, Massachusetts, 1954), pp. 294–370.
 - ³⁷T. Abe, Y. Takizawa, and S. Sato, 45th Aerospace Sciences Meeting and Exhibit, Reno, NV, 2007 (unpublished), AIAA Paper No. 2007-0187.